CORE-CONCRETE MOLTEN POOL DYNAMICS AND INTERFACIAL HEAT TRANSFER

CONF-861002--8

A. S. Benjamin*

Abstract

Theoretical models are derived for the heat transfer from molten oxide pools to an underlying concrete surface and from molten steel pools to a general concrete containment. To accomplish this, two separate effects models are first developed, one emphasizing the vigorous agitation of the molten pool by gases evolving from the concrete and the other considering the insulating effect of a slag layer produced by concrete melting. The resulting algebraic expressions, combined into a general core-concrete heat transfer representation, are shown to provide very good agreement with experiments involving molten steel pours into concrete crucibles.

Nomenclature

English Symbols

B	Parameter in equation for slag viscosity, Eq. (25)
c_p	Specific heat at constant pressure
D_h	Hydraulic diameter of liquid annulus, $2(R_s - R_b)$
g	Acceleration of gravity
Gr_L	Grashoff number based on characteristic length L
h	Heat transfer coefficient
H_{eff}	Effective heat of ablation
h_{fg}	Latent heat of vaporization
h_{NC}	Heat transfer coefficient for natural convection

*Sandia Laboratories, Albuquerque, New Mexico 87185; Member, ASME.

k	Thermal conductivity
$\dot{m}_{sf}$	Mass injection flux of slag components
p	Static pressure
Pr	Prandtl number, $\mu c_p/k$
$\dot{q}$	Heat flux
r	Radial coordinate
R_b	Radius of gas bubble
R_c	Radius of curvature at bottom of pool containment
R_d	Radius of slag droplet
Re_D	Reynolds number in liquid annulus, $\rho_f \bar{u} D_h/\mu_f$
R_s	Radius of symmetry, Figure 2(b)
T	Temperature
$\bar{T}$	Reference temperature for slag viscosity calculation
t_b	Characteristic passage time of a bubble, $2R_b/u_b$
ΔT_{sat}	Wall superheat, $T_w - T_{sat}$
T_w	Temperature at liquid-solid or slag-solid interface
u	Velocity component in principal direction
$\bar{u}$	Mean velocity in liquid annulus relative to liquid-bubble interface
u_b	Bubble rise velocity
u_s	Liquid velocity at $r = R_s$ (negative)
v	Velocity component in transverse direction
v_{cr}	Superficial vapor generation velocity at boiling crisis
v_e	Velocity at edge of boundary layer
v_g	Superficial gas injection velocity
v_o	Maximum value of v_e
v_{sf}	Superficial slag generation velocity
x	Coordinate parallel to surface

y	Coordinate transverse to surface
z	Axial coordinate in cylindrical system
z_o	Distance from wall to center of vortex, Figure 4(c)

Greek Symbols

δ	Thickness of slag layer
δ^*	Height of slag droplet at time of separation, Figure 9(b)
θ	Angle of inclination of solid surface
λ	Most probable wavelength for Taylor instability
μ	Dynamic viscosity
ν	Kinematic viscosity
ρ	Density
σ	Surface tension
τ_I	Shear stress at liquid annulus/bubble column interface
ϕ	Reference temperature weighting factor, Eq. (29)

Subscripts

b	Bubble
d	Droplet
g	Gas
ℓ	Liquid
s	Circle of symmetry
$s\ell$	Slag
v	Virgin material
1	Relating to Taylor instability problem for slag layer
2	Relating to creeping flow problem for slag layer
*	Maximum heat transfer condition

1. INTRODUCTION

If a core meltdown accident were to occur in a light water reactor, a pool of hot molten core materials would be expected to come into contact with the concrete of the reactor cavity. The rate of penetration of this pool into the concrete is governed by many factors, including (1) the nature of the decomposition and melting of concrete, (2) the vigorous agitation of the molten pool by gases evolving from the concrete, and (3) the insulating effect of slag-like components produced by concrete melting. The first of these considerations has been studied elsewhere [1], and adequate models have been developed. Very little work, however, has been performed in the areas of molten pool dynamics and slag insulating effects, although a recent survey report by Blottner [2] has brought attention to the importance of the latter.

This paper will study the second and third problems mentioned above and will develop theoretical models for the heat transfer from molten oxide pools to an underlying concrete surface and from molten steel pools to a general concrete containment. To accomplish this, the paper will first develop two separate effects models, as described in the next two paragraphs.

In Section 2, the paper will examine the heat transferred from a liquid pool to an underlying surface with gas injection through the surface. A model of the pool dynamics and heat transfer mechanisms will be derived and agreement with experiement will be shown. The model will subsequently be used, in Section 4, to predict the heat transfer from a molten oxide pool to an underlying concrete surface, accounting for slag dissolution in the oxide pool.

In Section 3, the paper will consider the effects of a thin slag layer separating a metallic pool from the concrete. Equations will be developed to predict the thickness of the slag layer and the corresponding heat transfer coefficient as a function of position, and these equations will be used to predict the heat transfer from a molten steel pool to a concrete containment. The results at the containment centerline will be shown, in Section 4, to compare very favorably with experiments involving molten steel pours into concrete crucibles.

2. HEAT TRANSFER FROM A LIQUID POOL TO AN UNDERLYING SURFACE WITH GAS INJECTION THROUGH THE SURFACE

2.1 Background

Liquid-to-solid heat transfer at a horizontal surface with gas evolution at the interface has been of interest over the past 20 years, primarily because of its similarity to pool boiling. The problem is also applicable to such industrial processes as electrolysis, where a gas may be evolved at the surface of an electrode; and catalysis, where liquids may react on a catalytic surface to produce gaseous products.

The first experimental investigation into the problem was performed in 1960 by Gose [3], who considered the heat transfer characteristics of water, ethylene glycol, and two kinds of oil, subjected to air or helium injection from below. The pools were contained within cylindrical vessels, with the bottoms being porous to allow injection of the gases. In 1965, Akturk [4] performed experiments with air being bubbled through a porous horizontal disk into pools of water. In 1976, Kutateladze and Malenkov [5] performed experiments similar to Gose's, utilizing pools of water and glycerine-water solutions with injection of nitrogen, helium, hydrogen, or argon.

A review of heat transfer correlations for bubble-agitated systems is given by Hart [6] and by Blottner [2]. In 1966, Konsetov [7] provided a theoretical attempt at predicting the heat transfer coefficient by using known heat transfer correlations for other flow configurations with the characteristic parameters adjusted to correspond to the bubbling liquid system. The results are not strictly applicable to the problem at hand because they do not account for mass transfer at the liquid-solid interface.

The similarities and differences between pool bubbling and pool boiling data are interesting to observe when the data are presented in the form of heat transfer coefficient, h, versus superficial gas velocity, v_g. Such a comparison is made in Figure 1, where heat transfer data for water pools with gas injection through the underlying surface are compared with pool-boiling data [8] obtained with the use of a horizontal heating element in a saturated pool. The superficial gas velocity, v_g, and heat transfer coefficient, h, for the pool boiling data were inferred from the reported heat transfer rates and surface temperatures via the relations $v_g = \dot{q}/\rho_g h_{fg}$ and $h = \dot{q}/\Delta T_{sat}$.

The analogy between the bubbling problem and the boiling problem through much of the nucleate boiling region ($0.04 < v_g < 0.15$ m/s) is readily apparent in Figure 1. Although this correspondence of results has been observed by other researchers [5,9], what has sometimes been overlooked is that the mechanisms leading to the maximum heat transfer coefficient and subsequent film formation are considerably different. In the boiling case, the maximum heat flux (or "pool boiling crisis") is governed by a Helmholtz instability at the gas liquid interface [10], leading to the formation of a stable gas film that attenuates the heat transfer coefficient by well over an order of magnitude. Both the boiling crisis and the film boiling process are significantly affected by the coupling between the gas generation rate and the wall superheat, and neither is strongly affected by the viscosity of the liquid. In the bubbling case, the maximum heat transfer coefficient is governed by the dynamics of the liquid and is sensitive to the liquid viscosity. Although a gas film is observed to form when the superficial velocity is high enough [5], the film remains so thin as to have no dramatic effect on the heat transfer to the underlying surface (Figure 1).

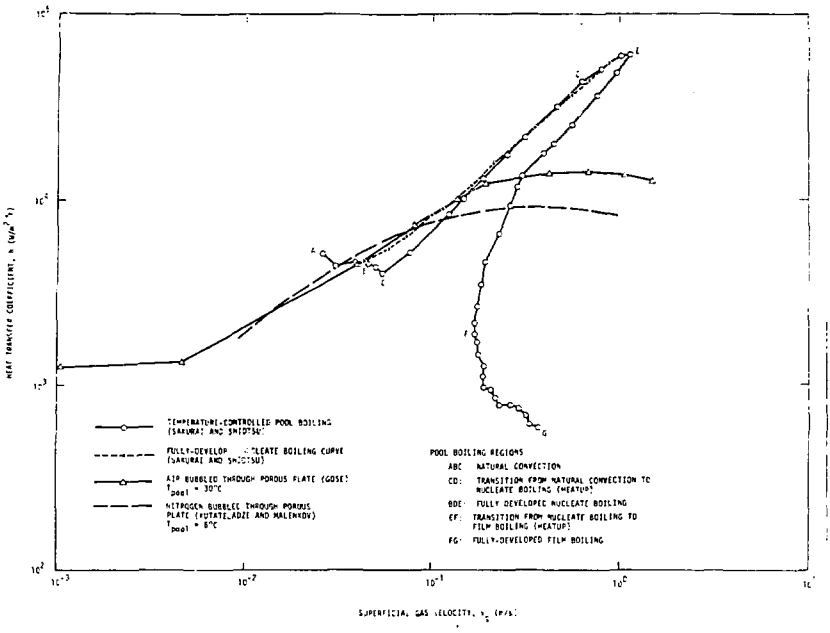

FIG. 1. COMPARISON OF SATURATED POOL BOILING AND GAS INJECTION HEAT TRANSFER FOR HORIZONTAL SURFACES IN WATER POOLS

The formulation of a theory for the liquid-to-solid heat transfer problem with relatively high rates of gas injection depends upon an adequate representation of the viscous flow, which will be considered next.

2.2 Pool Dynamical Model

To formulate a model of fluid and heat transport within a liquid pool that is agitated by gas bubbles, it is necessary to consider the fact that a turbulent flow situation probably exists. The presence of turbulent eddy-type motions is not known *a priori* but can be shown to be likely for most liquids on the basis of Reynolds number arguments to be presented later.

To the extent that turbulence is judged to be important, attempts to formulate a "physically exact" model from first principles are likely to be unprofitable. It seems more reasonable at the current stage of development to set up an approximate model that accounts for the important physical processes than to attempt

to solve the differential equations of two-phase-flow momentum and energy conservation, for example, by finite difference or finite element methods. In any such solution procedure, the approximate nature of the turbulent transport parameters would immediately compromise the accuracy of the results.

The approximate model is initially directed toward simulating the conditions existing in the pool at the precise superficial gas velocity, v_{g*}, that corresponds to the attainment of the peak heat transfer coefficient, h_*. To define the geometry of the bubble/pool mixture under these conditions, the rate of gas evolution is assumed to be sufficient to create a Taylor instability at the underlying surface. (The existence of a very thin gas film between the pool and the solid surface, implied by the Taylor instability assumption, is utilized only to estimate the bubble size and spacing. The film is considered to be too thin or too tenuous to affect the heat transfer significantly.)

The gas bubbles, then, evolve in an array of cylindrical columns [Figure 2(a)], which are spaced by the most probable wavelength [11]:

$$\lambda = 2\pi\sqrt{\frac{3\sigma}{g(\rho_\ell - \rho_{b_\ell})}} \tag{1}$$

For ease in formulating the equations, the square symmetry of the problem is replaced by a circular symmetry [Figure 2(b)], which is defined by the radius $R_s = \lambda/\sqrt{\pi}$. The radius of the bubble is given by $R_b = \lambda/4$; thus

$$\frac{R_s}{R_b} = \frac{4}{\sqrt{\pi}} \tag{2}$$

The maximum heat transfer to the underlying surface is postulated to occur when the rate of gas evolution is just sufficient to cause an incipient coalescence of bubbles in the column [Figure 2(a)]. That this condition corresponds to the maximum heat transfer rate is predicated on the position that further increases in v_g would cause the bubble columns to transform to jets. This would result in a net reduction of the buoyancy driving potential of the injected gas.

Since, for practical applications, the wavelength λ is quite small compared to the height of the pool, it is possible to divide the pool into the following regions: (1) a bulk region, where the flow is one-dimensional and fully-developed, and (2) localized regions near the boundaries of the pool where two-dimensional effects are important. Considering just the bulk region for now, the gas bubbles and entrained liquid in a cylindrical column are assumed to rise through the surrounding fluid with a common velocity, u_b [Figure 2(c)]. The liquid in the surrounding annulus

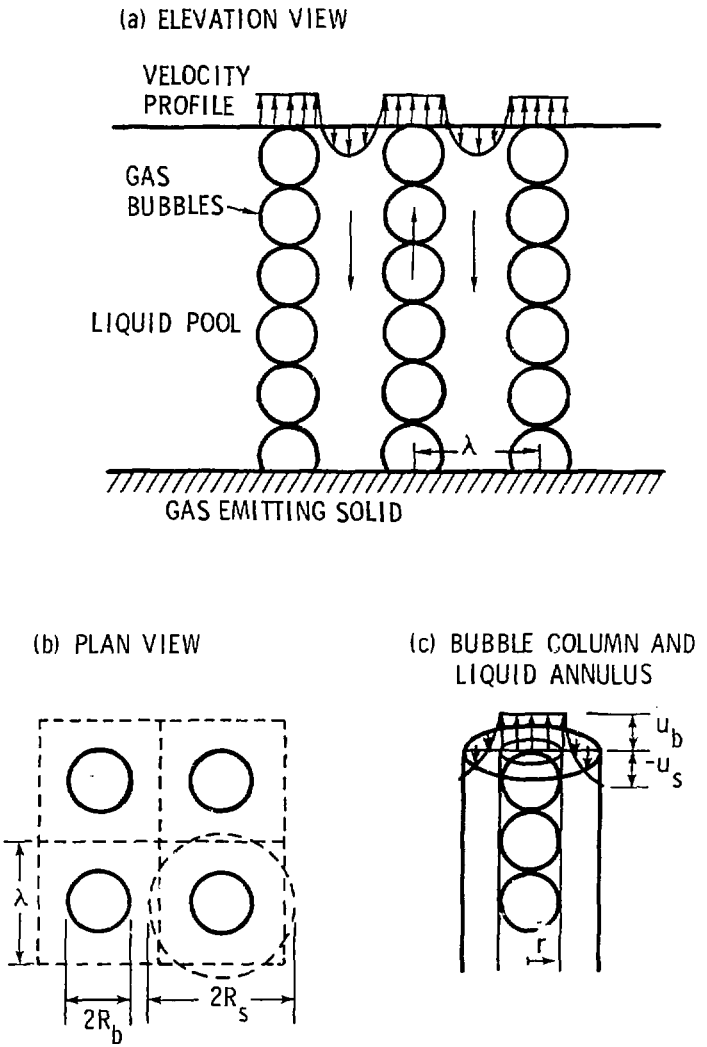

FIG. 2. POSTULATED GEOMETRY OF BUBBLE/LIQUID SYSTEM AT MAXIMUM HEAT TRANSFER CONDITION

accommodates itself to this environment by establishing a fully-developed velocity profile, which may be laminar or turbulent. This profile is assumed to be given by

$$u(r) = u_b - (u_s - u_b)\left(\frac{r - R_b}{R_s - R_b}\right)^{1/7} \tag{3a}$$

if the flow is turbulent, or by

$$u(r) = (u_b - u_s)\left(\frac{R_s - r}{R_s - R_b}\right)^2 + u_s \tag{3b}$$

if the flow is laminar. By analogy with flow in a pipe, the shear stress at the interface between the bubble column and the surrounding fluid is given by

$$\tau_I = 0.225\, \rho_\ell^{3/4}\, \mu_\ell^{1/4}\, (u_b - u_s)^{7/4} (R_s - R_b)^{-1/4} \tag{4a}$$

for turbulent flow, and by

$$\tau_I = 2\mu_\ell \frac{u_b - u_s}{R_s - R_b} \tag{4b}$$

for laminar flow.

The velocities u_b, u_s, and v_{g*} are obtained from the equations constituting conservation of mass for the gas phase, conservation of mass for the liquid phase, and conservation of momentum for the bubble column. Defining t_b as the transit time of a bubble passing through a horizontal plane, $2R_b/u_b$, these equations may be written, respectively, as

$$\pi R_s^2\, \rho_g v_{g*} t_b = \frac{4}{3}\pi R_b^3\, \rho_g \tag{5}$$

$$\left[\int_{R_b}^{R_s} 2\pi r\, u(r)\, dr\right] \rho_\ell\, t_b = -\left[(\pi R_b^2)(2R_b) - \frac{4}{3}\pi R_b^3\right] \rho_\ell \tag{6}$$

$$\frac{4}{3}\pi R_b^3\, (\rho_\ell - \rho_g) g = (2\pi R_b)(2R_b)\, \tau_I \tag{7}$$

Upon substitution of Equations (2) through (4) into Equations (5) through (7), the following equations result for v_{g*}:

Turbulent flow

$$v_{g*} = 0.523 \left(\frac{R_b}{\nu_\ell}\right)^{1/7} \left(gR_b \frac{\rho_\ell - \rho_g}{\rho_\ell}\right)^{4/7} \tag{8a}$$

Laminar flow

$$v_{g*} = 0.0185 \frac{gR_b^2}{\nu_\ell^2} \frac{\rho_\ell - \rho_g}{\rho_\ell} \tag{8b}$$

It may also be shown that $u_s = -1.57\ v_{g*}$ for turbulent flow, that $u_s = -3.66\ v_{g*}$ for laminar flow, and that $u_b = 7.64\ v_{g*}$ for both cases.

The determination of whether the flow is turbulent or laminar depends upon the Reynolds number of the liquid flow in the annulus surrounding the bubble column. The mean absolute velocity of this flow relative to the velocity at the interface between the column and annulus is

$$\bar{u} = \frac{1}{\pi (R_s^2 - R_b^2)} \int_{R_b}^{R_s} 2\pi r\ (u_b - u(r))\ dr \tag{9}$$

wherein, by utilizing Equation (6), it may be shown that $u = 8.26\ v_{g*}$. The Reynolds number based on this mean relative velocity and the hydraulic diameter of the annulus, namely, $Re_D = \rho_\ell\ \bar{u}\ D_h / \mu_\ell$, may be evaluated by using Equation (8), which leads to

Turbulent flow

$$Re_D = 35.4 \left(\frac{gR_b^3}{\nu_\ell^2} \frac{\rho_\ell - \rho_g}{\rho_\ell}\right)^{4/7} \tag{10a}$$

Laminar flow

$$Re_D = 1.25 \frac{gR_b^3}{\nu_\ell^2} \frac{\rho_\ell - \rho_g}{\rho_\ell} \qquad (10b)$$

Figure 3 illustrates the relationships derived in Equation (10) and shows the values of Re_D obtained for specific liquids of interest in the present study. It may be observed that the liquid hydrodynamics are predicted to be turbulent in all cases except for oil 69, concrete slag, and high-concentration glycerine solutions.

Using an analogy to flow in pipe, turbulent flow is presumed to exist if $Re_D > 2300$ and laminar flow if $Re_D < 2300$. As shown in Figure 3, a small ambiguity can sometimes occur if Re_D is greater than 2300 when evaluated from Equation (10a) and less than 2300 when evaluated from Equation (10b). Since the two equations intersect at $Re_D \approx 3000$, which is very close to the assumed transition Reynolds number, this ambiguity occurs very infrequently. It was not encountered in the cases considered for this paper and was therefore not considered further.

It is interesting to compare the superficial gas velocities of Equation (8) with the comparable value adopted by Zuber [10] as the superficial gas velocity at pool boiling crisis, viz.

$$v_{cr} = 0.0794 \left(gR_b \frac{\rho_\ell(\rho_\ell - \rho_g)}{\rho_g(\rho_\ell + \rho_g)} \right)^{1/2} \qquad (11)$$

It may be observed that Equations (11) and (8a) are quite similar in form, the main difference being the appearance of the factor $(\rho_\ell/\rho_g)1/2$ in Equation (11). The implication is that the velocity v_{g*} is much less sensitive to the density of the gas than the velocity v_{cr}, an implication that has been borne out by experiment.

2.3 Maximum Heat Transfer to the Underlying Surface

The heat transfer from the pool to its underlying surface is governed by a stagnation-point type of boundary layer flow [see Figure 4(a)]. The heat transfer coefficient for two-dimensional stagnation point flow can be expressed [12] as

$$h = 0.57 k_\ell \left(\frac{\rho_\ell (dv_e/dx)}{\mu_\ell} \right)^{1/2} Pr_\ell^{1/3} \qquad (12)$$

where x is the distance measured parallel to the surface from the stagnation point, and dv_e/dx is the velocity gradient of the inviscid flow at the edge of the boundary layer. The coefficient in

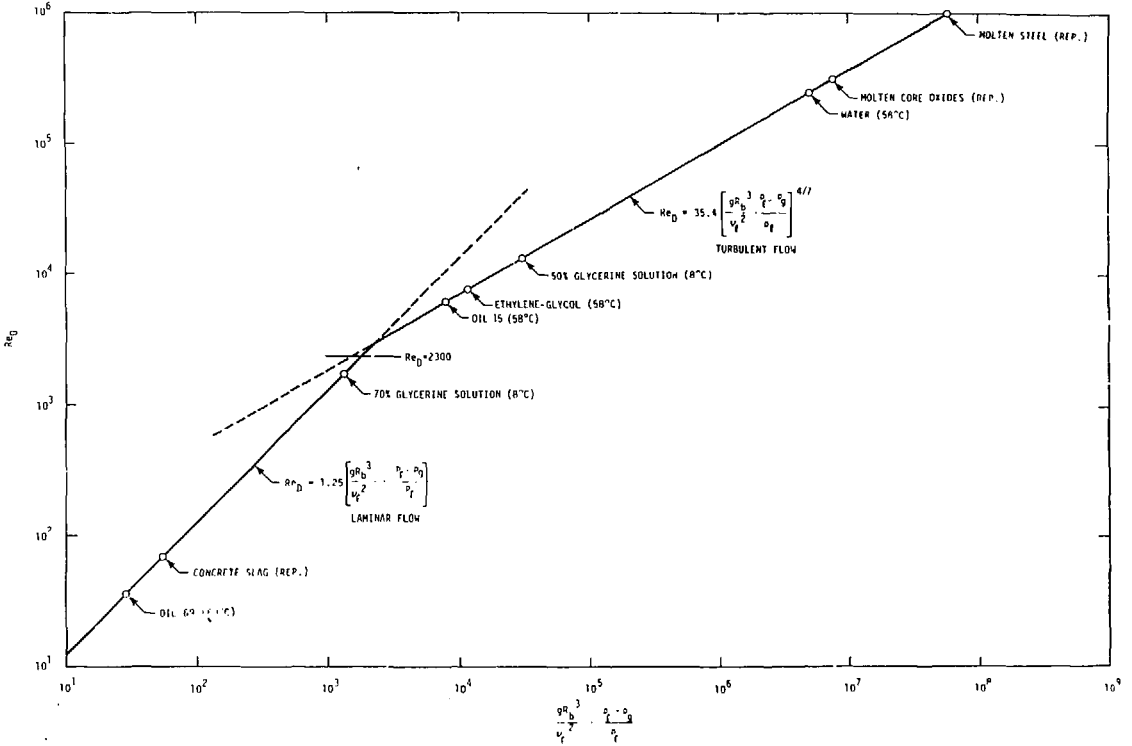

FIG. 3. LIQUID FLOW REYNOLDS NUMBER AT MAXIMUM HEAT TRANSFER CONDITION

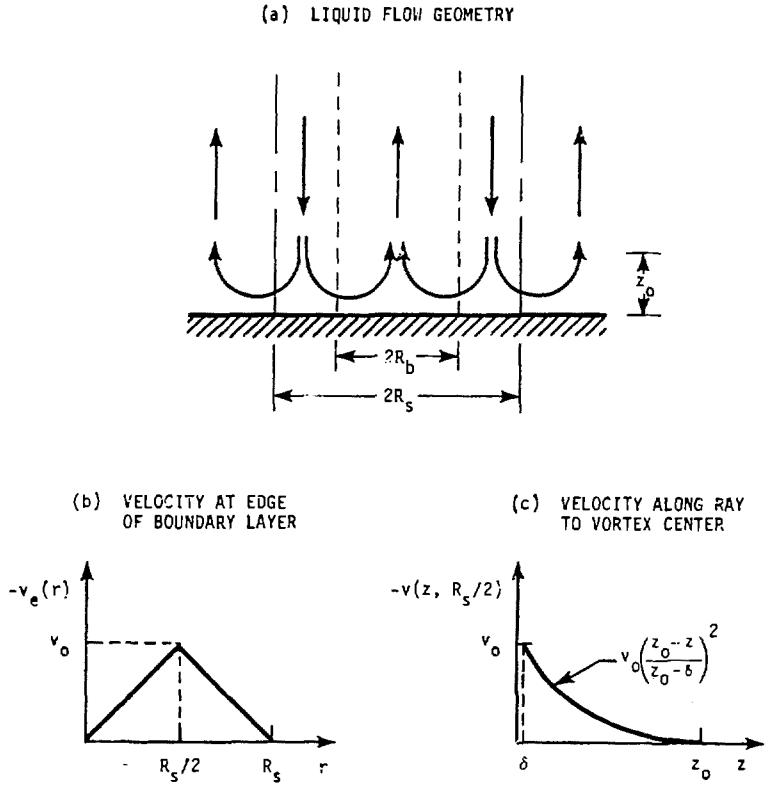

FIG. 4. ASSUMED NATURE OF THE FLOW NEAR THE UNDERLYING SURFACE

Equation (12) is sometimes increased by a factor on the order of 20% when the outer flow is turbulent. However, such a factor is considered small enough in the present context to be neglected.

In keeping with the approximate nature of the analysis, the velocity gradient will be estimated as follows. The radial velocity component at the edge of the boundary layer and that through the cylindrical element at $r = R_s/2$ will be assumed to have the forms shown in Figures 4(b) and 4(c), respectively. The vorticity at the edge of the boundary layer at $r = R_s/2$ will be taken to be equal to the average vorticity in the bulk region, viz.

$$\frac{2v_o}{z_o} = \frac{u_b - u_s}{R_s} \tag{13}$$

Conservation of mass requires that the horizontal mass flow through the cylindrical element at $r = R_s/2$ be equated to the liquid downflow in the annulus of the bulk region, viz.

$$\frac{\pi}{3} \rho_\ell v_o R_s z_o = -2\pi \rho_\ell \int_{r(u=0)}^{R_s} u(r)\, dr \tag{14}$$

Solving for v_o and using the assumed linear variation shown in Figure 4(b), the following expressions result for the velocity gradient at the edge of the boundary layer:

Turbulent bulk flow

$$\frac{dv_e}{dx} = 3.04 \frac{v_{g*}}{R_b} \tag{15a}$$

Laminar bulk flow

$$\frac{dv_e}{dx} = 4.45 \frac{v_{g*}}{R_b} \tag{15b}$$

Substituting Equation (15) into Equation (12) and utilizing Equation (8), the maximum heat transfer coefficient may be written as

Turbulent bulk flow

$$h_* = 0.562 \frac{k_\ell}{R_b} \left(\frac{g R_b^3}{\nu_\ell^2} \frac{\rho_\ell - \rho_g}{\rho_\ell} \right)^{2/7} Pr_\ell^{1/3} \tag{16a}$$

Laminar bulk flow

$$h_* = 0.218 \frac{k_\ell}{R_b} \left(\frac{g R_b^3}{\nu_\ell^2} \frac{\rho_\ell - \rho_g}{\rho_\ell} \right)^{1/2} Pr_\ell^{1/3} \tag{16b}$$

2.4 Heat Transfer as a Function of Superficial Gas Velocity: Comparison With Experiment

To obtain the full variation of heat transfer coefficient, h, over the plausible range of superficial gas velocities, v_g, and to compare the results with experiment, it is convenient to utilize the values of v_{g*} and h_* derived in Equations (8) and (16) as normalizing terms. For single-component pools at atmospheric pressure, excellent correlation of the data can be obtained over the full range of superficial velocities by using v_g/v_{g*} as the independent variable and $(h-h_{NC})/(h_*-h_{NC})$ as the dependent variable [Figure 5(a)]. Here h_{NC} is the turbulent natural convection limit of the heat transfer coefficient, which is taken to be

$$h_{NC} = 0.14 \frac{k_f}{L} (Gr_L Pr_f)^{1/3} \qquad (17)$$

Since Gr_L is proportional to L^3, the characteristic length, L, cancels out of the equation.

The significance of Figure 5 is not only that the data can be correlated by a single curve but also, since the curve passes through the coordinates (1,1), that the theoretically derived values of v_{g*} and h_* do closely represent the maximum heat transfer coefficient and the corresponding superficial gas velocity. Furthermore, because of the flatness of the correlation in the vicinity of its peak, only a 20% maximum error is incurred by approximating h as being equal to h_* for $0.35 < v_g/v_{g*} < 35.0$.

At pressures other than atmospheric, the correlation of Figure 5(a) changes somewhat in the region $v_g/v_{g*} < 1$ (see Figure 6). However, the derived maximum heat transfer coefficient, h_*, has been found to apply for all pressures and liquid/gas constituencies tested.

In the case of glycerine solutions in water [5] there appears to be a region of gas velocities where the effective solute fraction at the liquid-solid interface is higher than the nominal glycerine concentration in the bulk solution (see Figure 7). Previous researchers [3, 13] have attributed this type of behavior to an evaporation of solvent into the gas bubbles. Kutateladze and Malenkov presaturated their injection gases with water vapor, but apparently still experienced some type of solvent-to-bubble mass transfer.

3. HEAT TRANSFER FROM A LIQUID POOL TO AN UNDERLYING SURFACE WITH GENERATION OF AN IMMISCIBLE SLAG

3.1 Background

The residue of melting concrete is a viscous oxide slag whose composition is dependent upon the oxide mass fractions in the concrete being melted. Table 1 presents the mass fractions of the

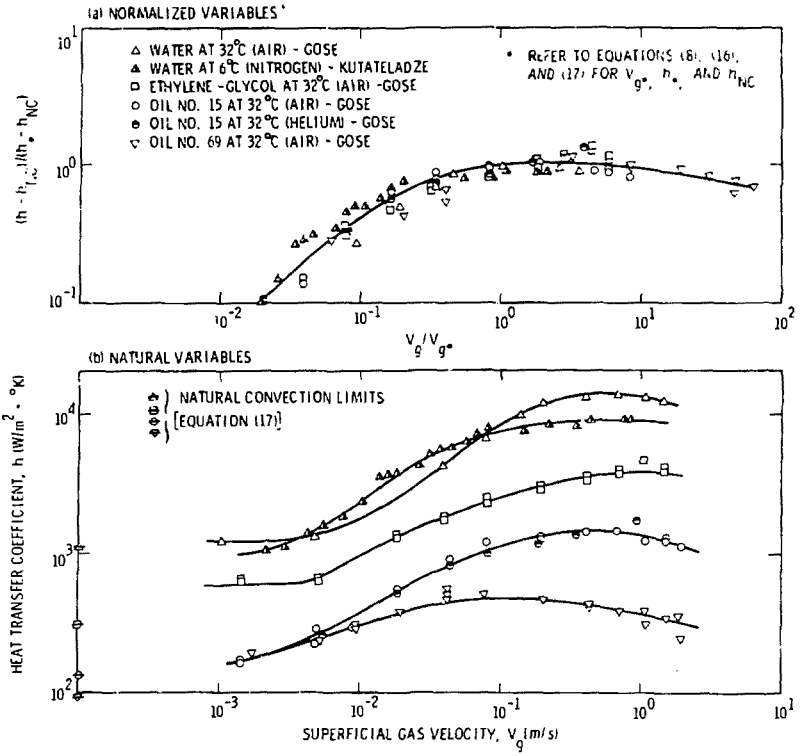

FIG. 5 HEAT TRANSFER COEFFICIENT VERSUS SUPERFICIAL GAS VELOCITY FOR VARIOUS LIQUID AND GAS COMBINATIONS AT AMBIENT PRESSURE

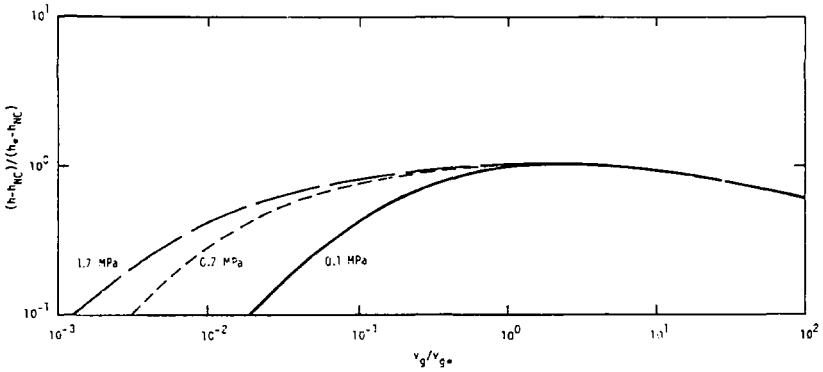

Fig. 6 EFFECT OF PRESSURE ON HEAT TRANSFER CORRELATION FOR SINGLE-COMPONENT POOLS

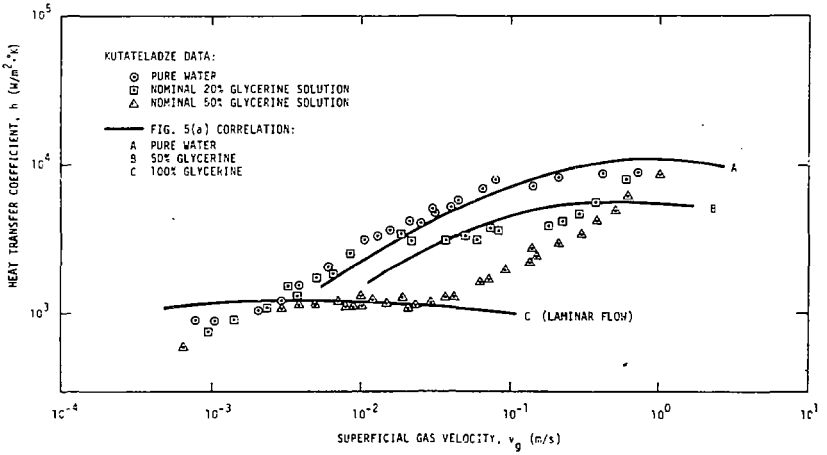

FIG. 7 COMPARISON OF CORRELATION WITH KUTATELADZE DATA FOR GLYCERINE-WATER SOLUTIONS

Table 1

Properties of Basaltic and Limestone Concrete

	Basaltic	Limestone
(a) Oxide Composition of Aggregate (Mass Fractions)		
SiO_2	0.592	0.483
CaO	0.095	0.422
Al_2O_3	0.090	0.049
Fe_2O_3	0.068	0.019
MgO	0.066	0.007
K_2O	0.058	0.017
Na_2O	0.020	0.001
TiO_2	0.011	0.002
Others	< 0.001	< 0.001
Total	1.000	1.000
(b) Heats of Ablation (cal/g)		
Loss of Evaporable Water	18	17
Loss of Chemically Bound Water	28	28
Decarboxylation	14	200
Melting	100	100
Sensible Heat	525	465
Total	685	810
(c) Other properties		
Solidus Temperature (°C)	1080	1150
Liquidus Temperature (°C)	1380	1400
Virgin Density (g/cm^3)	2.27	2.33

oxides existing in limestone and basaltic aggregate concrete, as well as some other concrete properties, and Figure 8 presents estimates of the viscosity of the slag as a function of its temperature.

In experiments involving molten steel pools in concrete crucibles [14], most of the slag produced by the concrete was observed after the test to constitute a thick, immiscible stratum overlying the denser steel pool. Posttest analyses also revealed that a thin slag residue remained on the surface of the crucible, separating the unmelted concrete from the steel pool. The thickness of these slag residues, roughly 2 to 3 mm, suggests that they contributed a significant resistance to the heat transport from the molten steel to the concrete.

The coexistence of a thick overlayer and a thin underlayer suggests a model of slag transport that is shown in Figure 9(a). The model consists of a combination of droplet formation and separation from the slag caused by a Taylor instability together with creeping movement of the slag around the sides of the containment. Both mechanisms contribute to the transport of slag to the upper stratum.

Because the viscosity of the slag is very large, it is possible to make two important simplifications. First, the agitation of the slag caused by the concrete decomposition gases can be neglected. Second, the inertia terms in the momentum equation can be omitted. The second simplification removes the nonlinear terms from the equation, making it possible for the Taylor instability and creeping flow problems to be treated separately and the results to be superimposed. Thus, the velocity components in the slag layer can be expressed as

$$\left.\begin{aligned} u(x,y) &= u_1(x,y) + u_2(x,y) \\ v(x,y) &= v_1(x,y) + v_2(x,y) \end{aligned}\right\} \quad (18)$$

where (x,y) is an axisymmetric coordinate system having $x = 0$ at the centerline of the concrete containment and $y = 0$ on the surface of the melting solid; $u_1(x,y)$ and $v_1(x,y)$ represent the velocity components in the slag layer corresponding to the Taylor instability problem; and $u_2(x,y)$ and $v_2(x,y)$ represent the corresponding velocity components for the creeping flow problem. An additional constraint is that

$$v_1(x,0) + v_2(x,0) = v_{sf} \quad (19)$$

where v_{sf} is the equivalent superficial slag generation velocity, $\dot{m}_{sf}/\rho_{sf}$.

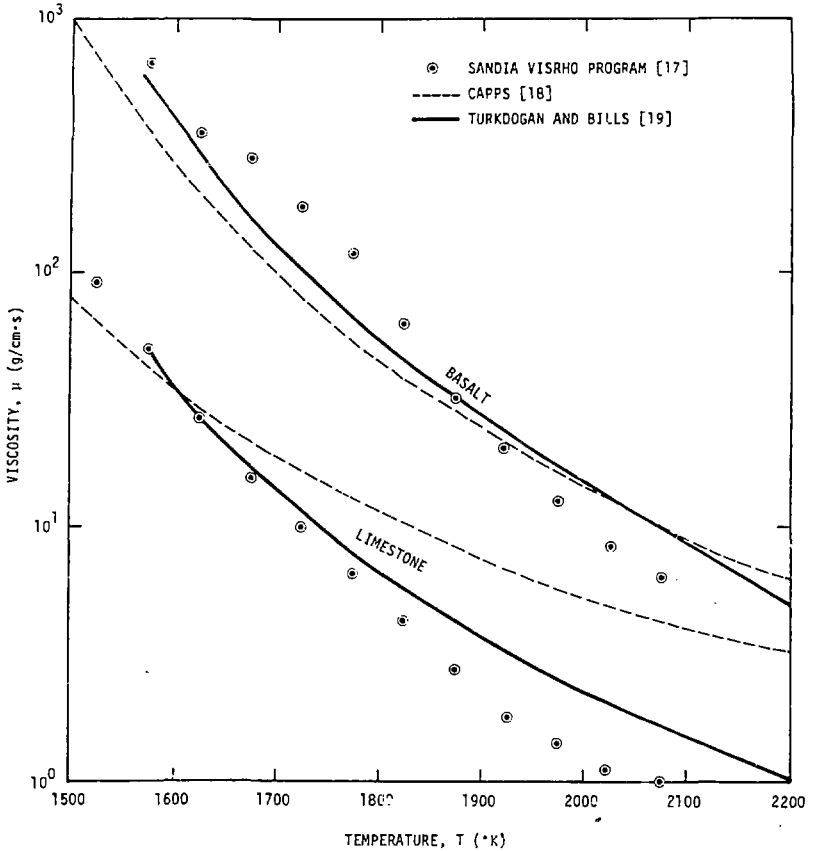

FIG. 8. VISCOSITY OF BASALT AND LIMESTONE SLAGS

(a) SLAG TRANSPORT MODEL

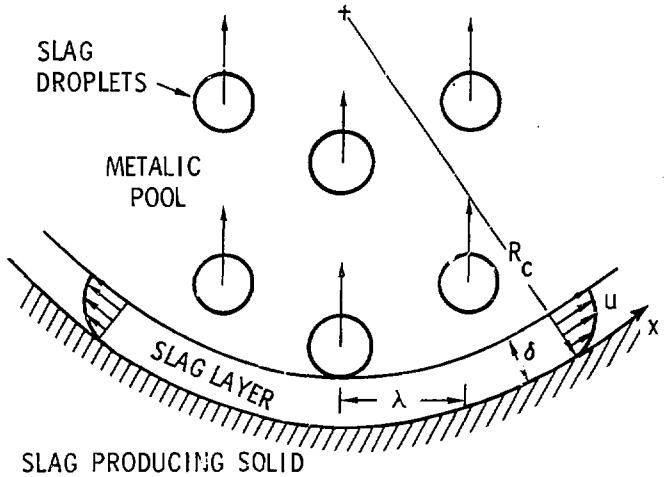

(b) GEOMETRY OF DROPLET FORMATION

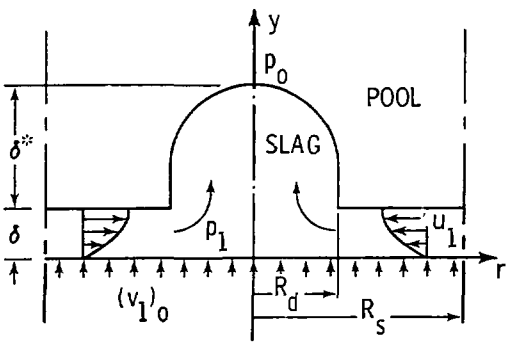

FIG. 9. SLAG TRANSPORT AND DROPLET FORMATION MODES

3.2 The Taylor Instability Problem

Consider first the Taylor instability problem, for which the hydrodynamical model is depicted in Figure 9(b). The problem has been solved previously by Berenson [11] and others [15], and so the main features only will be presented. The equations of mass and momentum conservation in the region $R_d \leq r \leq R_s$ can be written, respectively, as

$$\frac{1}{r}\frac{\partial}{\partial r}(ru_l) + \frac{\partial v_l}{\partial y} = 0 \tag{20}$$

$$\frac{\partial}{\partial y}\left(\mu_{s\ell}\frac{\partial u_l}{\partial y}\right) = \frac{\partial p_l}{\partial r} \tag{21}$$

and the boundary conditions can be written as

$$\left.\begin{aligned} y=0:\ & u_l=0,\ v_l=(v_l)_0 \\ y=\delta:\ & u_l=0,\ v_l=0,\ \partial u_l/\partial y=0 \end{aligned}\right\} \tag{22}$$

and

$$\left.\begin{aligned} r=R_d:\ & p_l = p_0 + \rho_\ell g\delta^* \\ r=R_s:\ & u_l=0,\ p_l = p_0 + \rho_\ell g\delta^* + \frac{2\sigma}{R_d} \end{aligned}\right\} \tag{23}$$

The second boundary condition at $y = 0$ is expressed in terms of the as-yet unspecified parameter, $(v_l)_0$, which is equivalent to $v_l(x,0)$ in Equation (20) and assumed to be uniform along $0 \leq r \leq R_s$. The zero shear-stress boundary condition at $y = \delta$ results from the slag viscosity being much higher than the viscosity of the liquid pool. The most probable wavelength for the case of two liquid layers is given by

$$\lambda = 2\pi\sqrt{\frac{2\sigma}{g(\rho_\ell - \rho_{s\ell})}} \tag{24}$$

rather than by Equation (1), but otherwise the relations $R_d = \lambda/4$ and $R_s = \lambda/\sqrt{\pi}$ still apply. In addition, $\delta* = \lambda/3$.

If it is assumed that the slag viscosity varies exponentially with temperature, viz.

$$\mu_{s\ell}(T) = \mu_o e^{-BT} \tag{25}$$

and that the temperature variation across the slag layer is linear, viz.

$$T = T_w + (T_\ell - T_w)\frac{y}{\delta} \tag{26}$$

then the following result may be obtained after integration of the conservation equations:

$$(v_1)_o = 0.295 \frac{(\rho_\ell - \rho_{s\ell})\, g\delta^3}{\mu_{s\ell}(\bar{T})\, R_d} \tag{27}$$

The reference temperature $\bar{T}$, in Equation (27), can be expressed as

$$\bar{T} = (1-\phi)T_w + \phi T_\ell \tag{28}$$

where

$$\phi = \frac{1}{B\Delta T} \ell n \left(\frac{e^{B\Delta T} - 1 - B\Delta T - \frac{1}{2}(B\Delta T)^2}{\frac{1}{6}(B\Delta T)^3} \right) \tag{29}$$

and $\Delta T = T_\ell - T_w$. Typically ϕ varies from 0.3 for relatively low temperature differences to 0.6 for high temperature differences. It is assumed that the temperature at the slag-liquid interface is equal to the temperature in the bulk of the liquid pool, by virtue of the high heat transfer coefficient from the pool to the slag interface, and that the temperature at the slag-concrete interface is equal to the average of the solidus and liquidus temperatures.

3.3 The Creeping Flow Problem

Consider next the creeping flow of the slag around the sides of the containment. The governing equations for this problem are

$$\frac{1}{r}\frac{\partial}{\partial x}(ru_2) + \frac{\partial v_2}{\partial y} = 0 \tag{30}$$

$$\frac{\partial}{\partial y}\left(\mu_{s\ell}\frac{\partial u_2}{\partial y}\right) = -(\rho_\ell - \rho_g) g \sin\theta \tag{31}$$

and the boundary conditions are

$$\left.\begin{array}{l} y=0: \quad u_2=0, \quad v_2=v_2(x,0) \\ y=\delta: \quad \partial u_2/\partial y=0, \quad v_2=0 \\ x=0: \quad u_2=0 \end{array}\right\} \quad (32)$$

Integration of the conservation equations in this case leads to

$$v_2(x,0) = \frac{(\rho_\ell-\rho_{s\ell})g}{3\,\mu_{s\ell}(\bar{T})\,r}\,\frac{d}{dx}\,(\sin\theta\; r\;\delta^3) \quad (33)$$

In the limit as $x \to 0$ and $\theta \to 0$ (i.e., at the bottom of the containment), Equation (33) becomes

$$(v_2)_o = \frac{2}{3}\,\frac{(\rho_\ell-\rho_{s\ell})\;g\delta^3}{\mu_{s\ell}(\bar{T})\;R_c} \quad (34)$$

where R_c is the radius of curvature of the solid surface at $x = 0$.

3.4 Heat Transfer Coefficient for the Combined Problem

The slag thickness at the containment bottom can be determined by summing Equations (27) and (34), substituting Equation (19), and solving for δ, viz.

$$\delta = 1.50\left(\frac{\nu_{s\ell}\;\mu_{s\ell}(\bar{T})}{(\rho_\ell-\rho_{s\ell})g}\;\frac{R_d\;R_c}{R_c+2.26R_d}\right)^{1/3} \quad (35)$$

The heat transfer coefficient across the slag layer at the containment bottom is given by $h = [(R_s^2 - R_d^2)/R_s^2] \cdot (k_{s\ell}/\delta)$, which leads to

$$h = 0.53\,\frac{k_{s\ell}}{R_d}\left[\frac{(\rho_\ell-\rho_{s\ell})\;gR_d^{\,2}}{\nu_{s\ell}\;\mu_{s\ell}(\bar{T})}\left(1+2.26\frac{R_d}{R_c}\right)\right]^{1/3} \quad (36)$$

Away from the origin at $x = 0$, the prediction of slag thickness and heat transfer coefficient as a function of x is complicated by a lack of information on the behavior of the Taylor instability at inclined angles. As a first approximation it may be assumed that Equation (28) is valid up to a small specified value

of θ, say 15°, and that thereafter the process of droplet formation and separation terminates. The variation of δ with x can thus be determined by integrating the equation

$$\frac{d}{dx}\left(\sin\theta\ r\ \delta^3\right) + 0.89\ \frac{r}{R_d}\ \delta^3 = \frac{3\ \mu_{s\ell}(\bar{T})\ r}{(\rho_\ell - \rho_{s\ell})g}\ v_{s\ell} \qquad (37)$$

up to $\theta = 15°$, and then integrating a corresponding equation without the term $0.89(r/R_d)\delta^3$ for $\theta > 15°$.

The determination of δ and consequently h depends upon an evaluation of the superficial slag generation velocity, $v_{s\ell}$, which usually requires the use of a computer code, such as that developed by Knight [1]. The physics contained in such codes can be rather detailed, including such considerations as the in-depth thermal response of the slag-producing solid, the internal decomposition reactions, and the transport of the gaseous products through the internal pore structure. To neglect these physics would generally not be advisable. In the present case, however, the heat transfer coefficient is inversely proportioned to only the cube root of the slag generation velocity [Equation (36)], so that a 50% estimation error, for example, in $v_{s\ell}$ would produce only a 14% corresponding error in h. Thus if a concrete response code is not available, it is permissible to approximate $v_{s\ell}$ by introducing an effective heat of ablation, H_{eff}, that accounts for the sensible heat, $c_p(T_w - T_o)$, the heat of melting, H_{melt}, and the heats associated with all the decomposition reactions in the concrete. Then by substituting the approximation

$$v_{s\ell} \approx \frac{h\ (T_\ell - T_w)}{\rho_v\ H_{eff}} \qquad (38)$$

into Equation (36), the heat transfer coefficient for the bottom of the containment can be shown to be equal to

$$h = 0.63\ \frac{k_{s\ell}}{R_d}\left[\frac{(\rho_\ell - \rho_{s\ell})\ g R_d^3\ \rho_v\ H_{eff}}{\mu_{s\ell}(\bar{T})\ k_{s\ell}\ (T_\ell - T_w)}\left(1 + 2.26\frac{R_d}{R_c}\right)\right]^{1/4} \qquad (39)$$

A similar approximation may be made for the remaining portions of the slag-producing solid.

4. CORE-CONCRETE HEAT TRANSFER MODEL AND COMPARISON WITH EXPERIMENT

Molten pools resulting from a core meltdown can include both a metallic phase and an oxide phase that, it is believed, would separate into two immiscible strata. Initially, the oxide stratum, consisting primarily of fuel and zirconium oxides, forms the

bottom layer of the pool, and the less dense metallic stratum, consisting mainly of molten steel, lies atop it. With the generation of large amounts of slag oxides, which are soluble with the molten core oxides, the oxide stratum becomes less dense than the metallic stratum and the two reverse positions. The slag products generated when the concrete contacts the molten steel pool are postulated to form an unstable thin layer, from which slag is gradually transported to the upper oxide stratum by the mechanisms described in Section 3. The physical properties of the molten steel, the molten core oxides, and the slag are given in Table 2.

Table 2

Estimated Properties of Molten Core and Slag Materials

	Molten Steel 1700°K	Molten Steel 2800°K	Molten Core Oxides	Concrete Slag
ρ_ℓ (g/cm^3)	6.9	6.4	7.8	2.5
μ_ℓ (g/cm·s)	0.060	0.017	0.040	See Fig. 7
k_ℓ (W/cm·K)	0.173	0.208	0.033	0.013
$c_{p,\ell}$ (J/g·K)	0.78		0.50	1.0
σ (dyn/cm)	~1500		~450	~300

When the molten core first contacts the underlying concrete surface, the heat transfer coefficient from the pool to the concrete can be calculated from the gas-agitated pool model, Equation (16), with the liquid properties being those of the molten core oxides. The corresponding heat transfer coefficient, shown as curve (b) in Figure 10, is on the order of 40,000 W/m^2·K. (The implied invariance of the heat transfer coefficient with pool temperature for this case is artificial and merely reflects that the variations of the oxide properties with temperature are unknown.) Subsequently, the heat transfer coefficient diminishes substantially as the slag oxides produced by concrete melting dissolve in the pool of core oxides. The lower limit of the heat transfer coefficient is shown as curve (c) in Figure 10, which was calculated from the gas-agitated pool model, Equation (16), by assuming that the liquid properties in the equation are those of the slag. Considering that the concentration of slag components is likely to become quite high near the bottom of the oxide pool, even though the components are miscible, curve (c) is currently presumed to govern for most of the period of concrete-oxide interaction. This presumption, however, has not yet been substantiated experimentally.

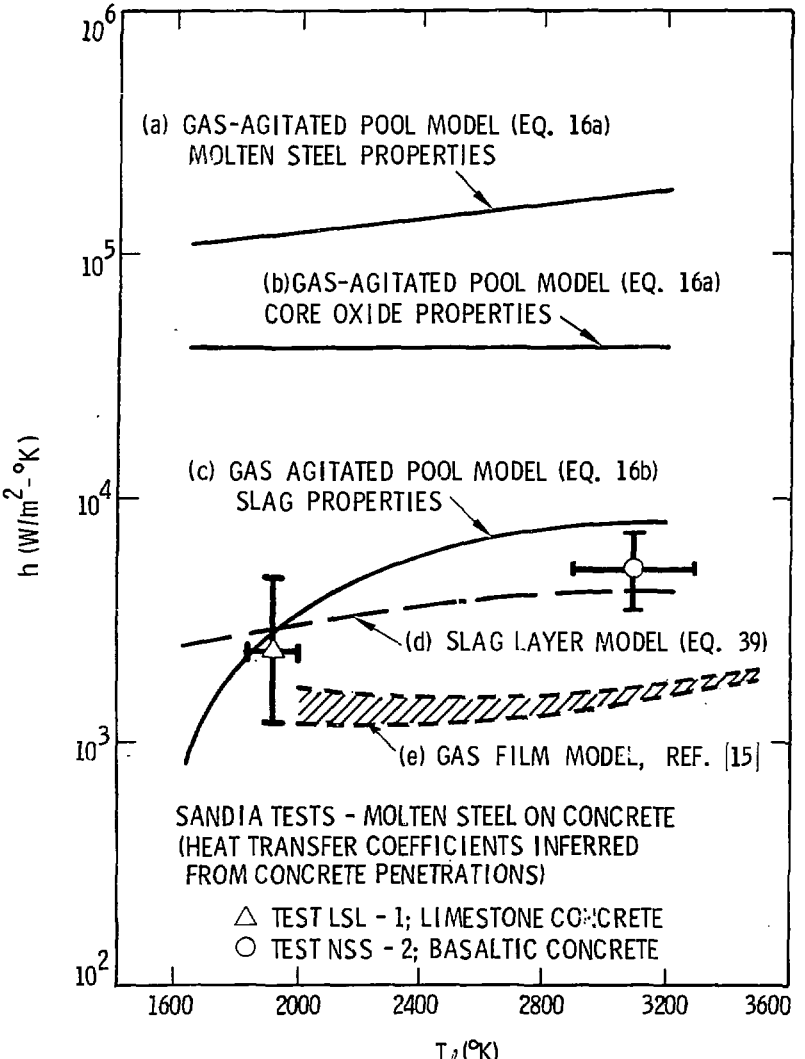

FIG. 10. DOWNWARD-DIRECTED HEAT TRANSFER COEFFICIENT VERSUS MOLTEN POOL TEMPERATURE

When the molten steel layer assumes the bottom position, the gas-agitated pool model, Equation (16), is assumed to provide the heat transfer coefficient from the molten steel bulk region to the interface with the slag layer (see curve (a) in Figure 10), and the slag layer model, Equation (39), provides the heat transfer coefficient from the interface to the underlying concrete surface [see curve (d)]. As shown in Figure 10, the slag layer contributes the larger thermal resistance (lower heat transfer coefficient) by nearby two orders of magnitude, and thus the temperature variation in the steel can be neglected.

Also shown in Figure 10 are two data points obtained from tests at Sandia Laboratories. In the large-scale test, LSL-1, approximately 200 kg of molten steel were poured into 61-cm diameter, hemispherical, limestone concrete cavity [14] whereas in the small-scale test, NSS-2, approximately 12 kg of steel were introduced into a 12.4-cm diameter, flat-bottomed, basaltic concrete crucible [16]. The heat transfer coefficients for these tests were estimated by evaluating the concrete surface recession rates from either real-time ultrasonic measurements (test NSS-2) or posttest visual observation (test LSL-1) and applying them, together with the concrete property data of Table 1, parts (b) and (c), in the equation $h \approx \rho_v \dot{s} H_{eff}/(T_\ell - T_w)$. Despite the large uncertainties in the data, as illustrated by the error bars, it is clear that the slag layer model reasonably reproduces the magnitude and temperature dependence of the data.

As a concluding remark, previous attempts [15] to explain the core-concrete heat transfer characteristics in terms of a gas-film resistance between the pool and the concrete are here called into question. Unlike pool boiling, where the heat transfer coefficient decreases sharply during the transition to film boiling (Figure 1), the heat transfer coefficient in a liquid pool with forced gas injection is not reduced significantly as the superficial gas velocity is increased beyond the point of maximum heat transfer. There is no evidence in these data of the high heat transfer resistances predicted by the gas film model. Finally, the gas film model severely underpredicts the inferred molten steel-concrete heat transfer data at high pool temperatures [Figure 10, curve (e)]. This underprediction of the heat transfer coefficient (i.e., overprediction of the resistance) is caused by the strong influence of thermal radiation in preference to conduction in the gas film model.

Acknowledgements

The author wishes to express his appreciation to Dr. F. G. Blottner, who was the first to identify the importance of the slag products in resisting the heat transfer form the molten pool to the solid concrete. Dr. Blottner also served as a most helpful

reviewer and provided useful background information. The author also wishes to thank Drs. D. A. Powers and J. F. Muir for reviewing this work and providing their own considerable insights.

References

1. Knight, R.L., "Thermal Behavior of Concrete," ANS Transactions, 27, Nov. 1977, pp. 528-529.

2. Blottner, F.G., Hydrodynamic and Heat Transfer Characteristics of Liquid Pools with Bubble Agitation, SAND79-1132, Sandia Laboratories, Sept. 1979.

3. Gose, E.E., Heat Transfer to Liquids with Gas Injection Through the Boundary Layer, Ph.D. Thesis, U.C. Berkeley, 1960.

4. Aktürk, N.U., "Heat Transfer from a Heated Porous Surface to a Pool of Liquid with Gas Injection at the Interface," Proc. Symposium on Two-Phase Flow, 2, Devon, England, June 1965, pp. 501-520.

5. Kutateladze, S.S., and I.G. Malenkov, "Fluid- and Gasdynamical Aspects of Heat Transfer in the Injection Bubbling and Boiling of Liquids," High Temperature, 14, 1976, pp. 703-711.

6. Hart, W.F., "Heat Transfer in Bubble-Agitated Systems: A General Correlation," Ind. Eng. Chem., Process Des. Dev., 15, 1976, pp. 109-114.

7. Konsetov, V.V., "Heat Transfer During Bubbling of Gas Through Liquid," Int. J. Heat Mass Transfer, 9, 1966, pp. 1103-1108.

8. Sakurai, A., and M. Shiotsu, "Temperature-Controlled Pool-Boiling Heat Transfer," Heat Transfer 1974, 4, Proc. 5th Intern. Heat Transfer Conf., Tokyo, 1974, pp. 81-85.

9. Sims, G.E., and P.L. Duffield, "Comparison of Heat-Transfer Coefficients in Pool Barbotage and Saturated Pool Boiling," The Engineering Journal, 14, May 1971, pp. 1-11.

10. Zuber, N., Hydrodynamic Aspects of Boiling Heat Transfer, USAEC Report AECU-4439, Ph.D. Thesis, U.C.L.A., 1959.

11. Berenson, P.J., "Film Boiling Heat Transfer from a Horizontal Surface," J. Heat Transfer C, 83, 1961, pp. 351-358.

12. Kayes, W.M., Convective Heat and Mass Transfer, McGraw Hill, 1966.

13. Dunskus, T., and J.W. Westwater, "The Effect of Trace Additives on the Heat Transfer to Boiling Isopropanol," Chem. Eng. Prog. Symp. Ser., 57, pp. 173-181.

14. Powers, D.A., et al., Exploratory Study of Molten Core Material/Concrete Interactions, July 1975-March 1977, SAND77-2042, Sandia Laboratories, 1978.

15. Alsmeyer, H., and M. Riemann, "On the Heat and Mass Transport Process of a Horizontal Melting or Decomposing Layer Under a Molten Pool," Nuclear Reactor Safety Heat Transfer, Winter Annual Mtg. ASME, 1977, pp. 47-53.

16. Sutherland, H.J., "Acoustic Measurement of the Penetration of a Molten Metallic Pool into Concrete," Nuclear Technology, to be published.

17. Powers, D.A., and A.W. Frazier, VISRHO: A Computer Subroutine for Estimating the Viscosity and Density of Complex Silicate Melts, SAND76-0649, Sandia Laboratories, June 1977.

18. Capps, W., "Some Properties of Cool Slags of Importance to MHD," 16th Symp. Engr. Aspects of MHD, 1977.

19. Turkdogan, E.T., and P.M. Bills, "A Critical Review of Viscosity of $CaO-MgO-Al_2O_3-SiO_2$ Melts," Ceramic Bulletin, 39, 1960, pp. 682-687.